
THERMOHALINE MIXING AND EXTINCTION IN STARS

Report submitted for the application for transfer from M.Phil. to Ph.D.

Alexander Lisboa-Wright

Astrophysics Research Institute, Liverpool John Moores University
September 2018

Abstract

So far in this project, the potential effects of thermohaline mixing in red-giant branch star models have been studied and their projected effect on local mass fractions of ^{14}N has been calculated. This effect is deemed to be highly significant, which will allow for the full implementation of thermohaline mixing in the models. The impact of fundamental stellar parameters on the ratio of values of interstellar extinction in different telescope filters has also been studied. The impact is significant and has been partially modelled using simple functions of the stellar parameters, a process which is ongoing at the time of writing.

Chapter 1

Introduction and background

1.1 Thermohaline mixing

The first months of the project were dedicated to the study of thermohaline mixing. This effect, first studied in detail by Ulrich (1972) and Kippenhahn et al. (1980), is proposed as a solution to the problem of otherwise-unexpected chemical abundances at the surface of low-mass ($\lesssim 1.5M_{\odot}$) red giant branch (RGB) stars Cantiello & Langer (2010), during these stars' evolution after the first-dredge-up (FDU). Specifically, the abundance differences consist of an over-abundance of ^{14}N , together with lower-than-expected abundances of ^7Li and C , as well as a decrease in the $^{12}\text{C}/^{13}\text{C}$ ratio, in the stellar spectra. Taken together, this presents a scenario of more CNO-cycle and lithium-burning fusion product nuclei, which would be expected to remain in the inner regions of the star after the FDU, and fewer fusion reactants at the stellar surface. This would indicate an exchange of material between the RGB star's fusion shell and the surface. While these same changes also appear during the FDU, which is due to standard convection, they should not be occurring after the FDU unless a different mixing process is responsible. It should also be noted that the post-FDU chemical changes are greater than the earlier convective FDU changes (Denissenkov, 2010).

The goal of this project is, ultimately, to implement a routine for calculating the effects of thermohaline mixing in BaSTI (Pietrinferni et al. (2004), Pasian et al. (2008)), a 1D spherically-symmetric stellar interior model which produces both a detailed layered structural representation of a particular star at a series of ages in its lifetime and a summary of the most important fundamental properties, such as stellar mass, luminosity and radius, which are used to compare the models to observed properties of stars. The software can also use these models to produce isochrones at fixed metallicity (Pietrinferni et al., 2013) with predicted magnitudes of stars of different masses in various filter systems.

Mixing of material occurs due to local thermodynamic instabilities. For stars, this requires consideration of 4 thermodynamic quantities: pressure P , temperature T , density ρ and molecular weight, μ , as well as a coordinate system in which to operate. For simple stellar models, radial symmetry is assumed, allowing the system

to be reduced to the radial coordinate r , measured from the stellar centre. If we assume a fully-ionized plasma containing N atomic species, the local mean molecular weight can be calculated as:

$$\mu = \frac{1}{\sum_{i=1}^{i=N} (Z_i + 1) \frac{X_i}{A_i}}, \quad (1.1)$$

where, for each species i , Z_i is its proton number, A_i its atomic mass number and X_i its fraction by mass in the local region.

Let us consider a bubble of gaseous material in pressure-equilibrium with its surroundings and represent mixing as a significant change in the bubble's (radial) position on a significant time-scale, arising from small differences in the remaining 3 thermodynamic quantities between the bubble and its surroundings. For a non-rotating star, using a simple linear approach, together with the Archimedes principle, gives a set of 4 homogeneous differential equations for the (small) differences in P, T, μ and r (Equations (3.1)-(3.4) in Salaris & Cassisi (2017)). If Δx_i are the differences in the 4 parameters, taking the ansatz form $\Delta x_i = B_i e^{nt}$ allows for a solution as a 3rd-order polynomial in n (Equation (3.5) in Salaris & Cassisi (2017)), if the determinant of the relevant matrix (dependent of the values of the B_i) is zero. The Routh-Hurwitz stability criterion can then be applied to this polynomial to give a general solution for n . For a physically-unstable solution, the exponent in the Δx_i equation must be positive, i.e. n must satisfy the condition $\text{Re}(n) > 0$. Hence, the subsequent constraints on the polynomial coefficients form all the possible conditions for instability, of which at least one must be satisfied. These constraints take the following form:

$$\nabla_\mu < 0 \quad (1.2)$$

$$\nabla_{\text{rad}} > \nabla_{\text{ad}} \quad (1.3)$$

$$\nabla_{\text{rad}} > \nabla_{\text{ad}} + \left(\frac{\phi}{\delta} \right) \nabla_\mu \quad (1.4)$$

where $\nabla_\mu = d \ln \mu / d \ln P$, $\nabla_{\text{rad}} = (\partial \ln T / \partial \ln P)_{\text{rad}}$ and $\nabla_{\text{ad}} = (\partial \ln T / \partial \ln P)_{\text{ad}}$ are the temperature-pressure gradients for the local environment (dominated by radiation pressure) and the bubble (treated as an adiabatic ideal gas), respectively, $\phi = (\partial \ln \rho / \partial \ln \mu)_{P,T}$ and $\delta = -(\partial \ln \rho / \partial \ln T)_{P,\mu}$ (Kippenhahn et al., 1980). For the case of this project, (ϕ/δ) is assumed to be positive, with a fixed value of 1, which is the result of applying the definitions of ϕ and δ to the equation of state for an ideal gas.

For convection to occur in a given stellar region, only Equation (1.3), known as the Schwarzschild criterion for instability, needs to be true.. Equation (1.4) is known as the Ledoux criterion. When there is a molecular weight inversion (thereby satisfying Equation (1.2)), instability arises invariably, but if only the Ledoux criterion is also true, the instability is thermohaline. If only the Schwarzschild criterion is true out of the three, the molecular weight gradient partially inhibits the effects of convective

instability. The mixing process in this case is known as semiconvection (Moore & Garaud, 2016).

The basic structure of low-mass RGB stars, starting from the physical centre of the star, can be summarised as follows:

1. Inert, electron-degenerate ${}^4\text{He}$ -dominated core (98% by mass), generally extending out to a coordinate fractional mass of $0.28M_{\star}$.
2. Fusion shell, in which the fusion reactions which previously occurred in the main-sequence core occur now in the RGB phase. The main reactions are the pp-chain and CNO cycle.
3. Radiative zone, consisting of layers for which the none of the instability criteria are fulfilled, thus ensuring stability against convection. For a solar-mass RGB star, this extends out to $0.29M_{\odot}$, as calculated both in the model generated for this work by BaSTI and by Eggleton et al. (2006), who employed a fully-3D hydrodynamic approach.
4. Convective zone, where the Schwarzschild criterion is fulfilled, and mixing is modelled using the mixing-length theory (MLT) (Salaris & Cassisi, 2017), with the free parameter modelled such that, given solar input parameters, the model produces solar outputs. Given the extremely short characteristic timescales for convective mixing, this process can be assumed to be instantaneous in full-stellar modelling.
5. Atmosphere, where the radiation is emitted from the star - this layer consequently dominates the nature of the emission (T_{eff} , emission lines, etc.)

Thermohaline mixing, as noted above, requires a molecular weight gradient inversion. This can be provided by the ${}^3\text{He}({}^3\text{He}, 2{}^1\text{H}){}^4\text{He}$ reaction, which is an unusual fusion reaction, as it maintains (very nearly) the same total nuclear mass while increasing the number of nuclei holding that mass. This decreases the local mean molecular weight and causes a gradient inversion between this layer and the layers above. Thermohaline mixing can be defined as a diffusive process (Kippenhahn et al., 1980), so it can be constructed in models to obey the diffusion equation for the mass fraction of atomic species i , X_i , as follows:

$$\frac{\partial X_i}{\partial t} = \frac{1}{\rho r^2} \frac{\partial}{\partial r} \left(\rho r^2 D \frac{\partial X_i}{\partial r} \right) \quad (1.5)$$

The strength of different diffusive effects in Equation (1.5) is dictated by their respective diffusion coefficient D . In the case of thermohaline mixing, the coefficient is defined (Cantiello & Langer, 2010) as:

$$D_{\text{thl}} = C_{\text{thl}} K \left(\frac{\phi}{\delta} \right) \frac{\nabla_{\mu}}{\nabla_{\text{rad}} - \nabla_{\text{ad}}} \quad (1.6)$$

where C_{thl} is a free parameter, which is set in this work to a value of $C_{\text{thl}} = 1000$, a value which gives consistency between the results of modelling the diffusion equation and observations of field (Charbonnel & Zahn, 2007) and globular cluster (Angelou et al. (2011), Angelou et al. (2012)) stars and K is the thermal diffusivity (Salaris & Cassisi, 2017), defined as:

$$K = \frac{4acT^3}{3\kappa\rho^2c_P} \quad (1.7)$$

where a is the radiation constant, c the speed of light, κ the Rosseland mean opacity and c_P the specific heat at constant pressure. Given the requirement for a molecular-weight inversion for thermohaline mixing to occur, D_{thl} was set to zero in the calculation if this criterion was not fulfilled.

1.2 Extinction

In the second part of the project, the effect of stellar properties on extinction values was studied. Extinction of light between a source object, such as a star, and a remote observer is subject to factors including the density and metallicity of the interstellar medium (ISM) along the emission travel path. However, stellar parameters (unrelated to distance or the ISM), including effective temperature T_{eff} , surface gravity g and metallicity Z , can significantly impact interstellar extinction as viewed in different filters. The result is that a stellar population's age, derived from CMDs, can differ significantly depending on whether or not these effects on extinction have been accounted for (Ortolani et al., 2017). Bolometric corrections represent mathematical estimates which account for the fact that, in a given filter, any part of the stellar spectrum outside the filter's wavelength range remains undetected by that filter. They are useful in all observations, in particular when observing objects visible only in a narrow spectral region.

After accounting for a general extinction effect on an object's emission, its apparent magnitude in a given filter X (i.e. wavelength range, which we define as increasing from λ_1 to λ_2) is given by:

$$m_X = -2.5 \log_{10} \left(\frac{\int_{\lambda_1}^{\lambda_2} f_{\lambda} (10^{-0.4A_{X,\lambda}}) S_{\lambda} d\lambda}{\int_{\lambda_1}^{\lambda_2} f_{\lambda}^0 S_{\lambda} d\lambda} \right) + m_X^0 \quad (1.8)$$

where f_{λ} represents the monochromatic flux at a given wavelength λ at the observer distance, $A_{X,\lambda}$ is the extinction value as a function of wavelength, S_{λ} is the response function and f_{λ}^0 and m_X^0 represent the monochromatic flux and apparent magnitude, respectively, of a known reference object in X . For the Gaia and Hubble WFC3 filter systems studied in this project, the star Vega was used as the reference object.

To derive the equation linking a bolometric correction with the extinction parameter, we start with the definition of a bolometric correction in a filter X , which is denoted by BC_X :

$$BC_X \equiv M_{\text{bol}} - M_X \quad (1.9)$$

where M_X is the absolute magnitude of the object in X and M_{bol} is its (predicted) absolute bolometric magnitude, defined relative to the Sun using:

$$M_{\text{bol}} = M_{\text{bol},\odot} - 2.5 \log_{10} \left(\frac{4\pi R^2 F_{\text{bol}}}{L_{\odot}} \right) \quad (1.10)$$

where F_{bol} is the bolometric stellar flux at its surface, R is the stellar radius, $M_{\text{bol},\odot}$ is the solar absolute bolometric magnitude, which is assumed in this work to have a value of 4.75 and L_{\odot} is the solar luminosity, for which a value of $3.844 \times 10^{33} \text{ erg s}^{-1}$ is used. Bolometric corrections can be expressed as a function of extinction using the universal definition of M_X in terms of m_X and the distance d to the source:

$$M_X = m_X - 2.5 \log_{10} \left(\left(\frac{d}{10 \text{ pc}} \right)^2 \right), \quad (1.11)$$

together with the equation $f_{\lambda} d^2 = F_{\lambda} R^2$, where F_{λ} is the monochromatic flux at λ at the stellar surface. This gives the final function for a bolometric correction for filter X :

$$\begin{aligned} BC_X = M_{\text{bol},\odot} - m_X^0 - 2.5 \log_{10} \left(\frac{4\pi R^2 F_{\text{bol}}}{L_{\odot}} \right) \\ + 2.5 \log_{10} \left(\frac{\int_{\lambda_1}^{\lambda_2} F_{\lambda} (10^{-0.4A_{X,\lambda}}) S_{\lambda} d\lambda}{\int_{\lambda_1}^{\lambda_2} f_{\lambda}^0 S_{\lambda} d\lambda} \right) \end{aligned} \quad (1.12)$$

For a filter X , the extinction parameter $A_X = A_{X,\lambda}$ must be calibrated relative to a known value. In this work we will input a value of the extinction in the well-studied Johnson- V filter, A_V . To extract A_X , we use the simple relation:

$$A_X = \left(\frac{A_X}{A_V} \right) A_V \quad (1.13)$$

together with the chosen value of A_V (for this project the values were $A_V = 0, 1$ - note that $BC_X(A_V = 0)$ effectively assumes no extinction), before taking the difference between the two $BC_X(A_V)$, giving the following equation:

$$\begin{aligned} BC_X(0) - BC_X(A_V) = 2.5 \log_{10} \left(\frac{\int_{\lambda_1}^{\lambda_2} F_{\lambda} S_{\lambda} d\lambda}{\int_{\lambda_1}^{\lambda_2} F_{\lambda} \left(10^{-0.4(A_{X,\lambda}/A_V)A_V} \right) S_{\lambda} d\lambda} \right) \\ \approx (A_X/A_V) A_V \end{aligned} \quad (1.14)$$

if $A_X = A_{X,\lambda}$ is assumed to be constant within the wavelength range of filter X , which is a valid assumption (Girardi et al., 2008), even for the wide-field Hubble filters being studied in this work.

Chapter 2

Current state of the field

2.1 Thermohaline mixing

Multiple studies have established the feasibility of thermohaline mixing as a solution for transporting species between the base of the convective zone and the H-fusion shell in low-mass RGB stars. Thermohaline mixing, arising from the ${}^3\text{He}({}^3\text{He}, {}^2\text{H}){}^4\text{He}$ reaction, can be sustained in models by initial molecular mass gradient inversions with relative changes as small as $(\Delta\mu/\mu) \sim 10^{-4}$ (Eggleton et al. (2006), Denissenkov (2010)). There were 2 slightly different approaches put forward for modelling thermohaline mixing:

1. Linear theory (Ulrich, 1972) - in a similar vein to the convection MLT, a simple linear model is assumed, one of the core assumptions being that the mixing occurs via radial movement of very thin regions (i.e. high aspect ratios). This allows the models of the mixing to remain one-dimensional and thus simplifies the calculation. The associated free parameter (C_{thl}) is constrained by observation examples.
2. Blob theory (Kippenhahn et al., 1980) - the same as the linear theory, with the exception of the elimination of the assumption that the blob of chemically-different material is narrow. This allows for non-linear effects to be considered, including flow patterns which cause the moving blob to mix into its surroundings, reducing and eventually removing the blob as a distinct object.

The difference between these two approaches, despite their identical underlying physical origin, was illustrated by Denissenkov (2010), in which agreement was found between that paper's 2D numerical simulation approach and the blob theory, while a simple linear analysis agreed with the linear theory. Both approaches used the same RGB object parameters, yet disagreed on the value of C_{thl} by at least 1 order of magnitude, with the linear approach giving the higher value. The value of 1000 for C_{thl} in this project is in agreement with the linear approach.

More generally, the theoretical approach to stellar interior mixing, including rotation, radiative levitation and thermohaline mixing, among other effects, is still a work in progress, with some disagreement regarding the implementation (Denissenkov (2010), Maeder et al. (2013)) and the numerical output (Lattanzio et al., 2015) of different simulation models.

2.2 Extinction

Many papers have examined the effects of extinction using ratios of reddening (a.k.a. colour excess) values as functions of wavelength primarily (Savage & Mathis (1979), Fitzpatrick & Massa (1988)). The seminal work in this field is Cardelli et al. (1989), hereafter CCM89, which fitted average ratios of the extinction parameter itself, rather than reddening ratios, to observational data from stars taken in the IR, optical (Cardelli et al., 1988) and UV (Fitzpatrick & Massa, 1988) spectral regions, as an empirical function of wavelength λ . They produced a basic universal equation of the form:

$$A_\lambda/A_V = a(x) + b(x)/R_V, \quad (2.1)$$

where $x \equiv 1/\lambda$ and $R_V \equiv A(V)/E(B - V)$. The total wavelength range was divided into 4 subranges, each with a governing pair of empirically-determined equations (to determine $a(x)$ and $b(x)$, respectively). The CCM89 model underpins more recent studies of intrinsic effects on extinction (Girardi et al. (2008), Casagrande & VandenBerg (2018b)), and provides the basis for the synthetic A_X/A_V dataset in this project.

ATLAS9 model atmosphere predictions (Castelli et al. (1997), Kurucz (1993)), calculated for a given value of stellar metallicity Z and a grid of 476 combinations of T_{eff} and $\log(g)$ values (Castelli & Kurucz, 2004) were used as synthetic stellar observation events.

Casagrande & VandenBerg (2018b), hereafter CV18b use a similar approach to this project for the 3 Gaia filters, extending the approach employed with other filter systems in Casagrande & VandenBerg (2018a), hereafter CV18a, i.e. deriving bolometric data from a library of synthetic stellar model atmospheres, then fitting the data to a model function to estimate the behaviour of the extinction as a function of stellar parameters. There are key differences between the two projects, however. Firstly, CV18a,b used MARCS model atmospheres instead of ATLAS9. More importantly, the metallicity and, particularly, T_{eff} ranges covered by CV18a,b were smaller than the ones covered in this project. This makes the results of this project more applicable for a wider range of T_{eff} values and therefore stellar population ages, particularly for the youngest such examples, such as open clusters, as shown by comparing Figures 4.7 and 4.8, which represent scenarios for open and globular clusters, respectively.

Chapter 3

Methodology

3.1 Thermohaline mixing

For modelling thermohaline mixing, the BaSTI (Pietrinferni et al. (2004)) 1D full-star, full-lifespan stellar evolution FORTRAN code was used. The initial model parameters are list in Table 3.1. The code was modified to calculate the impact, on both local radial layers and the overall star, of adding the effect of thermohaline mixing, on both short- and long-term time-scales. The software iterates through a series of variable time-steps between different model stellar objects, starting at a pre-determined phase of the stellar evolution sequence. The software reads in a file containing a pre-determined set of initial conditions, including initial stellar mass, helium mass-fraction Y and metallicity, as well as global settings, such as the total number of time-steps for which to generate models and whether to include different mixing effects. The mass fractions of the atomic species for the initial model (age, $t = 0$) were pre-calculated and stored in a separate file.

The object at each point in simulated time compromises a series of spherical layers, each with a local value of various physical parameters and of the mass fraction of all species being considered, representing the detailed physical and chemical structure of the stellar interior at that time.

So far in this project, the thermohaline mixing-related quantities were calculated using a routine separate from the main BaSTI code, which was run in its entirety prior

Input (initial) parameter	Value
Start time, ($t = 0$)	pre-MS
Mass	$1M_{\odot}$
Y	0.248
Z	0.0172 ($= Z_{\odot}$)
Diffusion	Enabled

Table 3.1: BaSTI initial setup

to employing the thermohaline routine. In this routine, all single differentials in a given layer k were calculated linearly as follows:

$$\frac{dy}{dx} = \frac{y_{k+1} - y_{k-1}}{x_{k+1} - x_{k-1}}, \quad (3.1)$$

a form known as the central difference method. To determine the potential for thermohaline mixing at a given model age, the abundances for all species in each layer were combined into a molecular weight value using Equation (1.1), then combined with the pressure of the same layer to produce the k th-layer value of ∇_μ via Equation (3.1). D_{thl} was then calculated using Equation (1.6), with a fixed value of $(\phi/\delta) = 1$ and the other parameters obtained directly from the BaSTI model's output tables. Equation (1.5) was then used, together with Equation (3.1) using the right-hand bracketed terms collectively as y , to give the time differential of the mass fraction. Since this is merely a first-order approximation test of the feasibility for thermohaline mixing, and since the central difference method throws up the possibility of a result of zero for a solitary positive- D_{thl} layer, the k th-layer value of D_{thl} was used for the diffusion equation. The k th-layer value of the mass-fraction as a function of time was then calculated using the following linear iterative equation:

$$X_{i,n,k} = X_{i,n-1,k} + \delta t \left(\frac{\partial X_i}{\partial t} \right)_k, \quad (3.2)$$

where n is the time iterator, with a maximum value of 100, and δt is the time-step, with a fixed value of 500yr, giving an overall simulation time-scale of 50,000 years.

3.2 Extinction

When calculating the bolometric corrections, the reference values taken by the parameters for Vega were:

1. $m_X^0 = 0.03$ for the Gaia filters
2. $m_X^0 = 0.00$ for the Hubble WFC3 filters

together with $M_{bol,\odot} = 4.75$. Equation 2.1, with the different wavelength regimes for $a(x)$ and $b(x)$ described by CCM89, was used with the A_V calibration values to simulate the extinction parameter in Equation 1.12. R_V was set to a value of 3.1, the standard value for the diffuse interstellar medium. The integration was carried out by iteratively adding the integrand results at regular small wavelength intervals. The non-zero calibration value of $A_V = 1$ was chosen, as this allows for significant changes in A_X/A_V from Equation (1.14), while also being close enough to zero to avoid significant changes in A_X/A_V due to the Forbes effect (Girardi et al., 2008).

This produced two tables of bolometric correction data, one for each value of A_V . The $A_V = 1$ data were then subtracted from the $A_V = 0$ using the approximation in

Parameter	Minimum	Maximum	Number of values
T_{eff}/K	3500	50000	76
$\log(g/\text{cm s}^{-1})$	0.0	5.0	11
$\log(Z/Z_{\odot})$	-2.0	0.5	4

Table 3.2: Stellar parameters values used in this project. Note: not all T_{eff} values have data for all $\log(g)$ values - see Castelli & Kurucz (2004) for details

Equation 1.14. This resulted in a single table of A_X/A_V values. It should be noted that, during this final subtraction, the m_X^0 and $M_{\text{bol},\odot}$ values at both A_V calibration values are the same, so the final results are unaffected by any errors in these values. The total range of parameter values used in this project can be found in Table 3.2. Although the ATLAS9 minimum T_{eff} value is 3500K, due to a low- T_{eff} artefact present in the data for several filters in both the WFC3 and Gaia systems, this project only analysed data for $T_{\text{eff}} \geq 4500\text{K}$. Coincidentally, this temperature cut also avoided any impact of the aforementioned Forbes effect due to low- T_{eff} values (less than 4000K, becoming especially prominent at 2500K, according to Girardi et al. (2008)).

Once the extinction data was produced, the next step was to attempt to mathematically describe the variations in A_X/A_V arising from the ATLAS9 stellar objects' effective temperatures, surface gravities and metallicities. This was done by creating mathematical functions of these stellar parameters and fitting these functions to the data, with the functions' coefficients being the free parameters whose values formed the results of the fit. The first stage within the fitting process was to assume the data to be a function of T_{eff} only. In this stage, extinction data at a fixed value of stellar surface gravity ($\log(g/\text{cm s}^{-1}) = 5.0$) and metallicity ($Z = Z_{\odot}$) was used for fitting. No anchor data points were used at this stage. The errors on the resulting values for the coefficients of A_1 were computed as a covariance matrix. The σ values for the coefficients displayed in Table 4.1 were extracted from the variances, which together form the leading diagonal of the covariance matrix. The results of this stage are stored in the function $A_1 = A_X/A_V(T_{\text{eff}})$. This function took on one of two function forms, each containing 3 free parameters (denoted by a , b and c), depending on the relative performance of both functions in each filter. The first case, referred to in Table 4.1 by the abbreviation 'pow', models a fit of the following power-law form:

$$A_{1,\text{pow}}(T_{\text{eff}}) = a(T_{\text{eff}})^b + c \quad (3.3)$$

while the second case (denoted by 'exp') models an exponential:

$$A_{1,\text{exp}}(T_{\text{eff}}) = a \exp(bT_{\text{eff}}) + c \quad (3.4)$$

The second fitting stage, whose results are stored as $A_2(T_{\text{eff}}, \log g, Z)$, was treated as a correction to the results of the first fitting stage. Not all filters required a second fitting, as seen in Table 4.2. Since the main variations generally arise from changes

in T_{eff} , the final output of results is a plot of A_X/A_V against T_{eff} . Given that the A_1 results remain consistent with the data at high T_{eff} values across all filters due to the data tending towards a constant value of A_X/A_V , an upper T_{eff} -limit of 8000K was set for A_2 as an anchor point for the function. The data for the fitting was obtained by taking the data used to fit A_1 ($Z = Z_{\odot}$, $\log(g)=5.0$) and subtracting from it the data at all other $\log(g)$ and Z values. The final model for the ratio of extinction parameters, A_{final} , was therefore defined as:

$$A_{\text{final}}(T_{\text{eff}}, \log(g), Z) = A_1(T_{\text{eff}}) + A_2(T_{\text{eff}}, \log(g), Z) \quad (3.5)$$

Given the issues encountered with modelling the A_2 functions, this project utilised the latest version of the BaSTI database (Hidalgo et al., 2018) to ascertain the range of $\log(g)$ values covered by the selected T_{eff} range.

Chapter 4

Results and Discussion

4.1 Thermohaline mixing

Using the methodology described in Section 3 and the BaSTI model described in Table 3.1, the thermohaline routine was applied to the output physical and chemical data at a model age of $\log_{10}(t/\text{yr}) = 10.10616695$ in simulated time, for which $\log_{10}(L/L_{\odot}) = 2.1231$. At this point, the star is in the RGB phase and, following the FDU and the subsequent recession of the convective envelope towards the surface, its interior structure has settled into the configuration detailed in Section 1.1. The species selected to trace the location and evolution of any thermohaline mixing event was ^{14}N . This selection was made on the basis of known changes in ^{14}N abundance as a function of temperature, and hence radius, within the fusion shell.

The radial gradients of all chemical species, the mean molecular weight, ∇_{μ} , D_{thl} and the time-evolution data for $X_{^{14}\text{N}}$ were calculated for each layer. Focussing on the region of the hydrogen-burning shell, the ^3He gradient is plotted against stellar radius in Figure 4.1, with the line colour corresponding to the local value of D_{thl} , as shown in the colour bar. For a known fusion region, the positive value of dX/dr for a species known to burn under the local conditions indicates that burning is indeed happening. The conclusion that can be drawn from Figure 4.1 is that the stellar region hosting the conditions required for thermohaline mixing (indicated by non-zero D_{thl}) and coincide with ^3He -burning, as expected. The values of D_{thl} are of the same order of magnitude as those found by Lattanzio et al. (2015).

For the same radial region, the mass fraction for ^{14}N is shown in Figure 4.3, with each line representing the mass-fraction profile at a different time, with specific times listed in the legend. The behaviour of the mass fraction in the left-hand side of the figure ($R \lesssim 0.055R_{\odot}$) matches the behaviour shown in Figure 1 of Charbonnel & Zahn (2007). The explanation for this two-step series is the domination of the CNO cycle in burning hydrogen in RGB fusion shells over the pp-chain, which dominates in MS core hydrogen burning.

The CNO cycle in low-mass stars consists of two separate cyclic branches, which create ^4He from ^1H via two different series of proton captures and β^+ decays involving

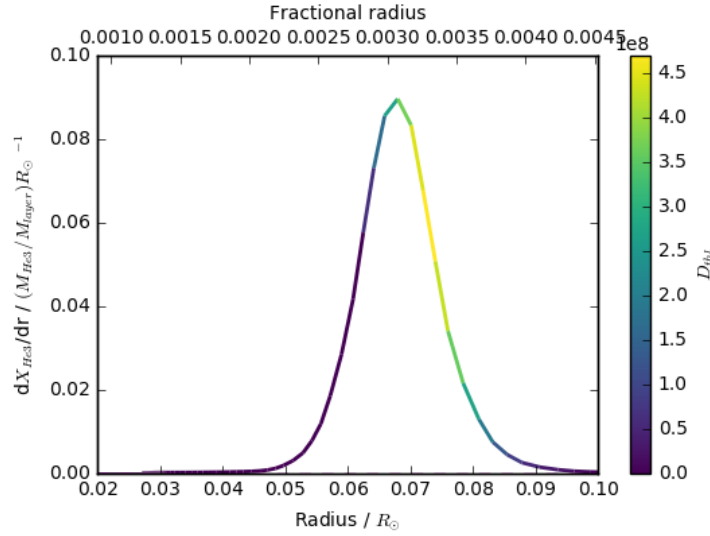
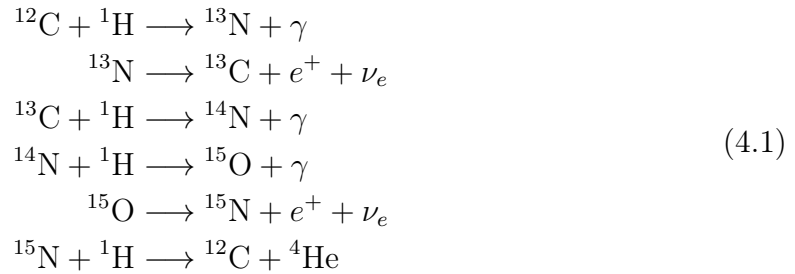
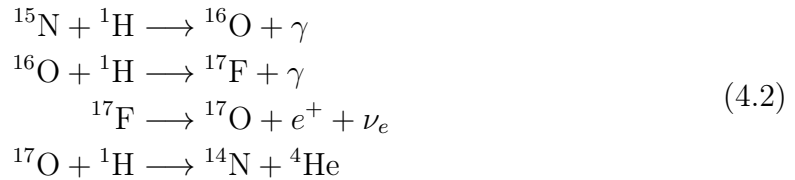


Figure 4.1: ${}^3\text{He}$ abundance gradient for model with $Z = Z_{\odot}$, $M = 1M_{\odot}$ and diffusion effects included, at a point $\log(L/L_{\odot}) = 2.1231$

isotopes of C, N and O as catalysts, with each isotope existing at an equilibrium abundance. In low-mass stellar cases, the CNO cycle is formed of two branches - the CN and NO cycles. The CN cycle-branch comprises (Salaris & Cassisi, 2005) the following series of steps:



The NO cycle-branch, which requires higher temperatures overall due to the higher mass and Coulomb-repulsion effects involved, comprises the following steps:



Focussing specifically on ${}^{14}\text{N}$, which is a stable isotope, the difference in its interactions between the branches is its parent nuclei. Each branch of the CNO cycle requires a temperature sufficiently high to support all its constituent fusion reaction

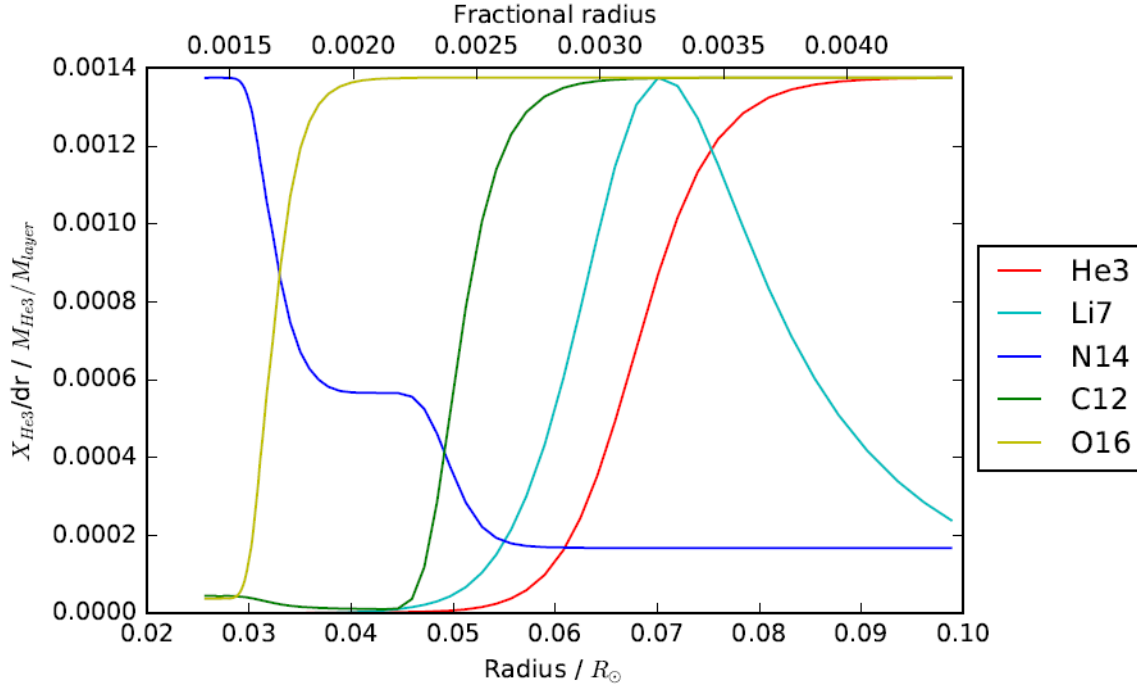


Figure 4.2: Mass fractions, with values normalised to those for ${}^3\text{He}$, for 5 species for model with $Z = Z_{\odot}$, $M = 1M_{\odot}$ and diffusion effects included, at a point $\log(L/L_{\odot}) = 2.1231$

steps. When this condition is no longer fulfilled, the production and destruction of the C, N and O isotopes is no longer in equilibrium. As temperature decreases with increasing radius, the first branch to reach this stage is the NO cycle, followed by the CN cycle. Once this stage is reached, reaction rates dictate how elemental abundances change. The NO cycle, which is a net producer of ${}^{14}\text{N}$, stops, leading to a drop in ${}^{14}\text{N}$ abundance at lower temperatures and a slight increase in ${}^{16}\text{O}$, which can be produced with ${}^{15}\text{N}$ from the CN cycle at temperatures lower than those required for oxygen fusion. At temperatures too low to sustain the CN cycle, the ${}^{12}\text{C}$ and ${}^{13}\text{C}$ can no longer be burned and hence the production of nitrogen is halted, leading to the second drop in ${}^{14}\text{N}$ abundance and an increase in carbon abundance. The normalised changes of the mass fractions of some of these species is shown in Figure 4.2, clearly showing the predicted behaviour for ${}^{12}\text{C}$, ${}^{14}\text{N}$ and ${}^{16}\text{O}$, as well as for ${}^7\text{Li}$ and ${}^3\text{He}$, both of which are burned in the H-burning shell, as expected.

The CNO-cycle cutoff location establishes the location of ${}^3\text{He}$ burning, as shown in Figure 4.1, as being in the outer part of the H-burning shell, which agrees with the predictions of other models and is closest to the radiation zone, where thermohaline mixing is hypothesised to take effect.

Furthermore, Figure 4.3 shows that, in a timespan of $5 \times 10^4\text{yr}$, of the order of the intervals between the ages of individual BaSTI models (10^4yr around the model considered in the plots), the projected effect of thermohaline mixing on the local mass

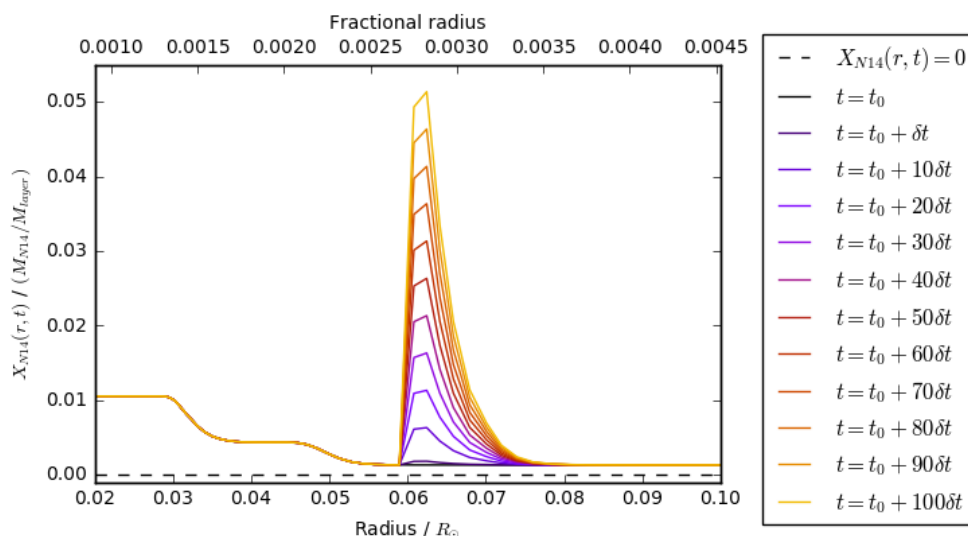


Figure 4.3: ^{14}N abundance time derivative for model with $Z = Z_{\odot}$, $M = 1M_{\odot}$ and diffusion effects included, at a point $\log(L/L_{\odot}) = 2.1231$

fraction of ^{14}N is highly significant.

As shown in Figure 4.3, the conditions for thermohaline mixing are reproduced in the BaSTI code. The location of the regions for which these conditions apply is located in the upper, and therefore cooler, layers of the hydrogen fusion shell, where ^3He burning occurs.

So far, by measuring abundances of species which both are hydrogen fusion products and are not involved in ^3He burning, such as ^{14}N , it has been established that the existing BaSTI stellar evolution model creates the conditions for thermohaline mixing to occur in the radiative zone of a low-mass, post-FDU RGB star. It has also been shown that, as expected, the conditions are created by molecular weight inversions arising from ^3He burning.

While the physical process and impacts of thermohaline mixing have been successfully implemented in other stellar evolution codes, such as MESA and STAREVOL, BaSTI has not yet been modified to include these in the iterative calculations. Achieving this is a significant goal because, as demonstrated by Lattanzio et al. (2015) in the particular case of lithium abundances, there can be significant differences in predictions of abundances between different stellar evolution codes. Adding BaSTI to the list of codes available for future comparative studies would provide more scope to study potential sources of error, such as the model time-step and C_{thl} value effects on abundances noted by Lattanzio et al. (2015). Of particular interest is the C_{thl} free-parameter value, as there are many proposed values, from authors using different approaches and models, which differ in some cases by at least an order of magnitude.

While the magnitude of the change due to thermohaline mixing in Figure 4.3 gives an idea of the region in which the effect arises, the figure does not show any actual

System	Filter	A_1 function	A_1 coefficients		
			a	b	c
WFC3	f218w	exp	-232.4 ± 48.1	$-(1.076 \pm 0.043) \times 10^{-3}$	2.933 ± 0.007
	f225w	exp	-128.5 ± 13.8	$-(1.031 \pm 0.022) \times 10^{-3}$	2.610 ± 0.003
	f275w	exp	0.9726 ± 0.0581	$-(3.518 \pm 0.109) \times 10^{-4}$	2.060 ± 0.001
	f300x	pow	$-(5.335 \pm 0.936) \times 10^5$	-1.664 ± 0.021	2.052 ± 0.001
	f336w	pow	$-(1.516 \pm 0.723) \times 10^4$	-1.582 ± 0.056	1.648 ± 0.001
	f390w	pow	-0.5991 ± 0.1494	-0.08071 ± 0.09090	1.738 ± 0.309
	f438w	pow	$-(1.000 \pm 0.463) \times 10^5$	-1.783 ± 0.054	1.352 ± 0.001
	f475w	pow	$-(1.207 \pm 0.379) \times 10^5$	-1.707 ± 0.037	1.220 ± 0.001
	f555w	pow	$-(4.560 \pm 1.490) \times 10^5$	-1.881 ± 0.038	1.080 ± 0.001
	f606w	pow	$-(3.137 \pm 0.911) \times 10^5$	-1.829 ± 0.034	0.9648 ± 0.0003
	f625w	pow	$-(5.476 \pm 3.709) \times 10^5$	-2.030 ± 0.079	0.8787 ± 0.0002
	f775w	pow	$-(6.328 \pm 4.571) \times 10^3$	-1.576 ± 0.085	0.6567 ± 0.0001
	f814w	pow	$-(3.727 \pm 1.381) \times 10^3$	-1.431 ± 0.044	0.6158 ± 0.0002
Gaia	G	pow	$-(3.381 \pm 0.733) \times 10^4$	-1.394 ± 0.026	1.040 ± 0.001
	G _{bp}	pow	-457.6 ± 64.9	-0.9000 ± 0.0172	1.247 ± 0.002
	G _{rp}	pow	$-(4.383 \pm 0.871) \times 10^3$	-1.361 ± 0.023	0.6771 ± 0.0002

Table 4.1: Coefficient values produced by A_1 fitting

mixing taking place, as Equation 3.2 does not allow for changes in mass fraction between layers and it assumes $(\partial X_i / \partial t)$ to be independent of time, so the current calculation does not give rise to a physically-viable diffusive effect. Cantiello & Langer (2010)

More fundamentally, the equation for D_{thl} itself is not beyond dispute. When thermohaline mixing is studied in the full context of a non-homogeneous medium, such as a hydrogen-burning shell, outside the moving material bubble, in the normal stellar case ($\nabla_\mu > 0$ for the medium) the molecular weight gradient acts to counter the thermohaline effect, leading to a modified equation for D_{thl} (Denissenkov, 2010).

4.2 Extinction

Table 4.1 shows the best results obtained for $A_{1,\text{exp}}(T_{\text{eff}})$ for all filters. All coefficient values are presented with a precision of 4 significant figures.

Using the results of Table 4.1, A_1 is plotted as a solid line, together with the original data, in Figure 4.4. The

As shown in Figures 4.5 and 4.6, for some filters, there are significant changes in the extinction ratio values at fixed T_{eff} ($|\delta A| > 0.02$), due to changes in $\log(g)$, Z or both.

Figure 4.7 shows the $T_{\text{eff}}\text{-}\log(g)$ plane for a BaSTI isochrone at solar metallicity for a stellar population with an age of 16 Myr, corresponding to a young open cluster. The

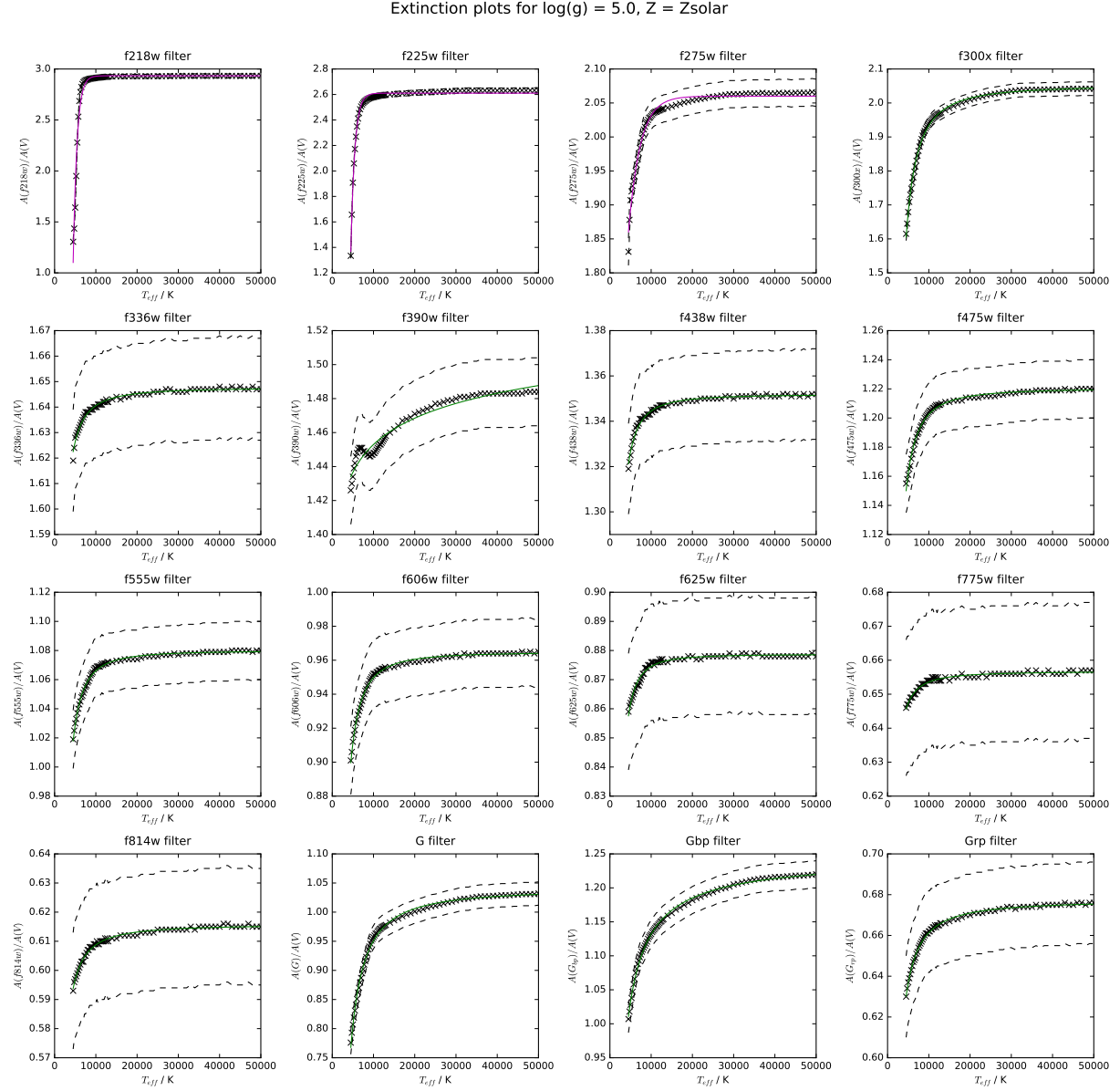


Figure 4.4: Plots of the best A_1 fitting result in each filter. Purple lines indicate that the fit took the form $A_{1,\text{exp}}$, while green lines indicate the same for $A_{1,\text{pow}}$. The dotted lines indicate deviations of ± 0.02 from the data (black crosses)

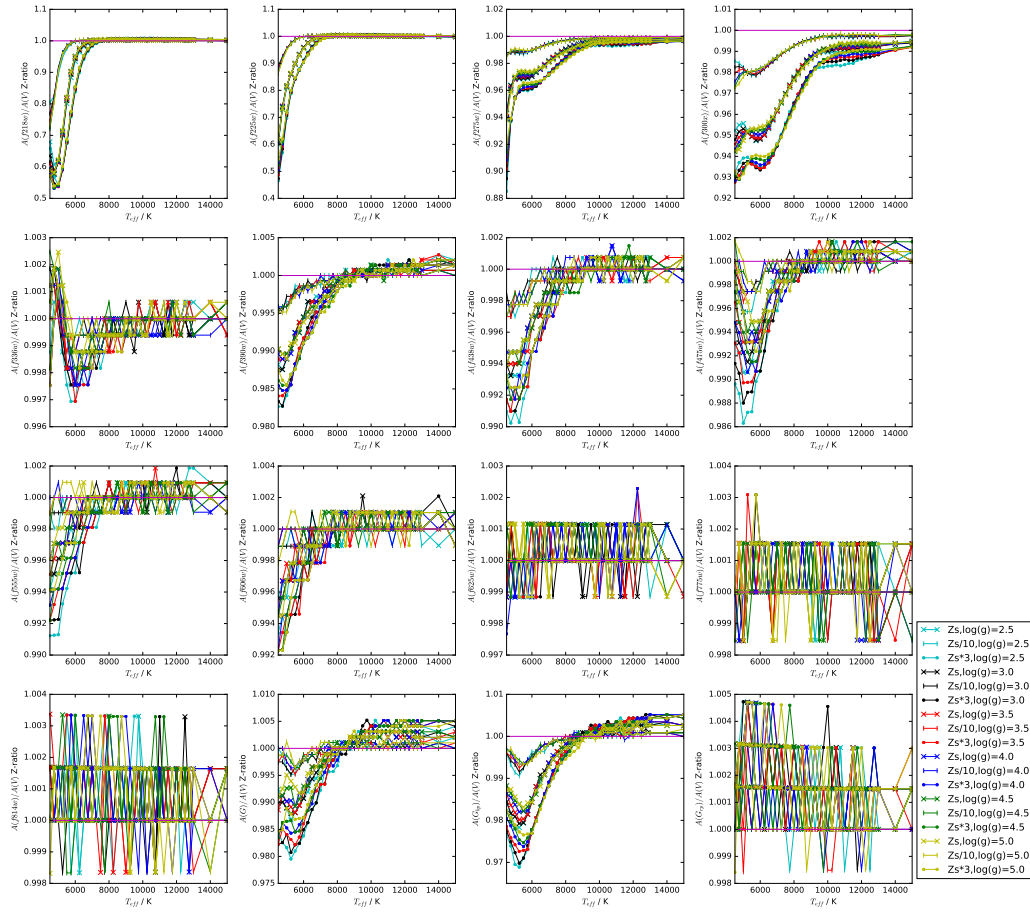


Figure 4.5: Ratios of A_X/AV values for different Z values compared with solar metallicity data at $\log(g) = 5.0$

objects included in the figure are limited to the region used for fitting the A_1 and A_2 functions, so any objects with $T_{\text{eff}} < 4500\text{K}$, i.e. the coolest giants and main-sequence dwarfs, are excluded. Combining the known variations of A_X/AV with $\log(g)$ and Z in the data used for fitting the functions with the known spread of the same parameters in the available isochrone data (Pietrinferni et al., 2013), it can be seen that A_2 fitting is necessary in some filter, as detailed in Table 4.2.

When fitting the A_1 functions, with the exception of the f218w, f225w, f275w and f300x filters (the shortest-wavelength filters, all in the UV), all fitting results were accurate to within ± 0.02 of the $\log(g) = 5.0$ data. From Figure 4.5, the same pattern occurs with metallicity, as the data for only the 4 aforementioned filters vary by more than 3%, even between the $\log(Z/Z_\odot) = -2.0$ and 0.5 data. The 4 filters with low-accuracy results will require additional terms in T_{eff} , i.e. a modified A_1 function, to mimic the data to an acceptable degree of accuracy. As shown in Figures 4.7 and 4.8, even when considering only BaSTI isochrone data with $T_{\text{eff}} \geq 4500\text{K}$, the range of

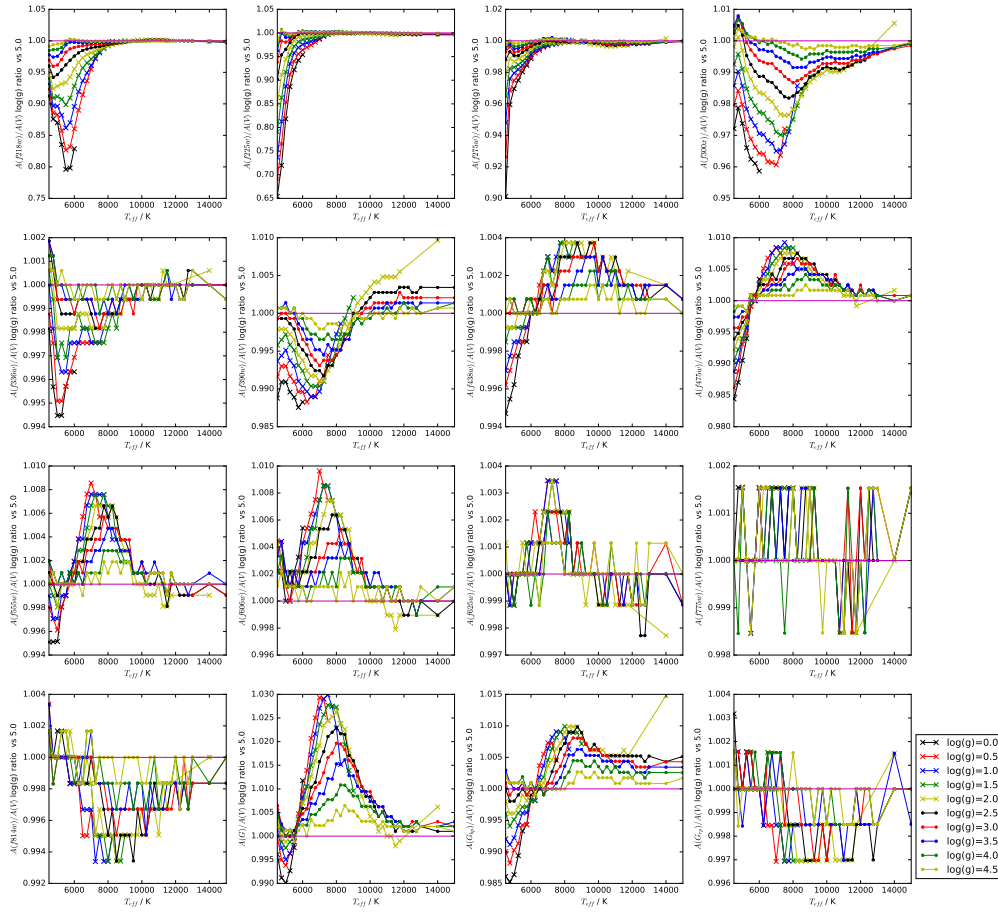


Figure 4.6: Ratios of A_X/AV values for different $\log(g)$ values compared with $\log(g) = 5.0$ data, all at solar metallicity

$\log(g)$ values covered still requires A_2 functions to be computed for the full range of isochrone ages, for those filters which require it, as shown by the significant changes in Figure 4.6, even for $\log(g) = 2.5$, which is inside the lower limit for the 10Gyr isochrone. The relative shapes of the individual curves suggests that a single function of $\log(g)$, moderated in magnitude by the T_{eff} of the data, could be obeyed by all of the curves. At the time of writing, this scenario is being studied using multiple forms of $A_2(T_{\text{eff}}, \log(g))$ below temperatures of 8000K. This apparent disagreement with the fitting function form described in Casagrande & Vandenberg (2018a) and Casagrande & Vandenberg (2018b) is simply due to the fact that the relevant filters were not studied in those works - this project agrees with those works for the filters studied both in those works.

The significant effect of metallicity is also, at the time of writing being investigated using A_2 functions, as this effect also occurs in the region $T_{\text{eff}} \leq 8000\text{K}$. This will follow the same approach as the $\log(g)$ -investigation.

System	Filter	A_2 required?
WFC3	f218w	Y
	f225w	Y
	f275w	Y
	f300x	Y
	f336w	N
	f390w	N
	f438w	N
	f475w	N
	f555w	N
	f606w	N
	f625w	N
	f775w	N
	f814w	N
Gaia	G	N
	G _{bp}	N
	G _{rp}	N

Table 4.2: Assessment of necessity for A_2 fitting

4.3 Conclusion

In this project so far, the physical conditions required for thermohaline mixing in low-mass RGB stars have been confirmed, and the projected effect of the mixing has been shown to be significant with regard to the local mass fraction of ^{14}N . The location of the initial mixing effect has also been localised to the region of ^3He burning. The project has also made progress towards modelling the effect of extinction as a function of fundamental stellar properties, with the largest variations accounted for using effective temperature alone, with more minor variations still being studied at the time of writing.

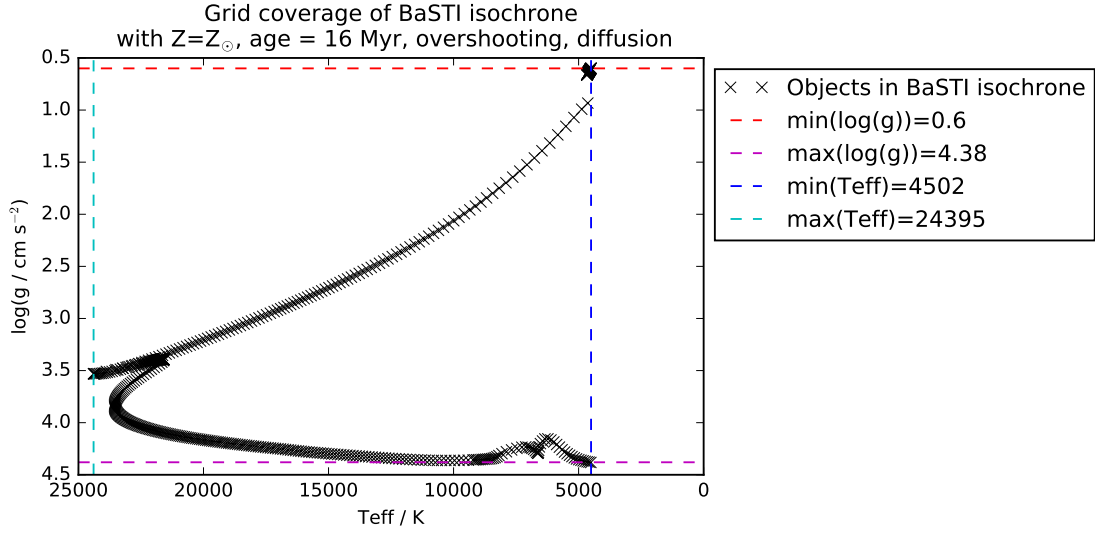


Figure 4.7: $T_{\text{eff}}\text{-log}(g)$ grid coverage by a 16 Myr, Z_{\odot} BaSTI isochrone including mass-loss, core overshooting and diffusion effects

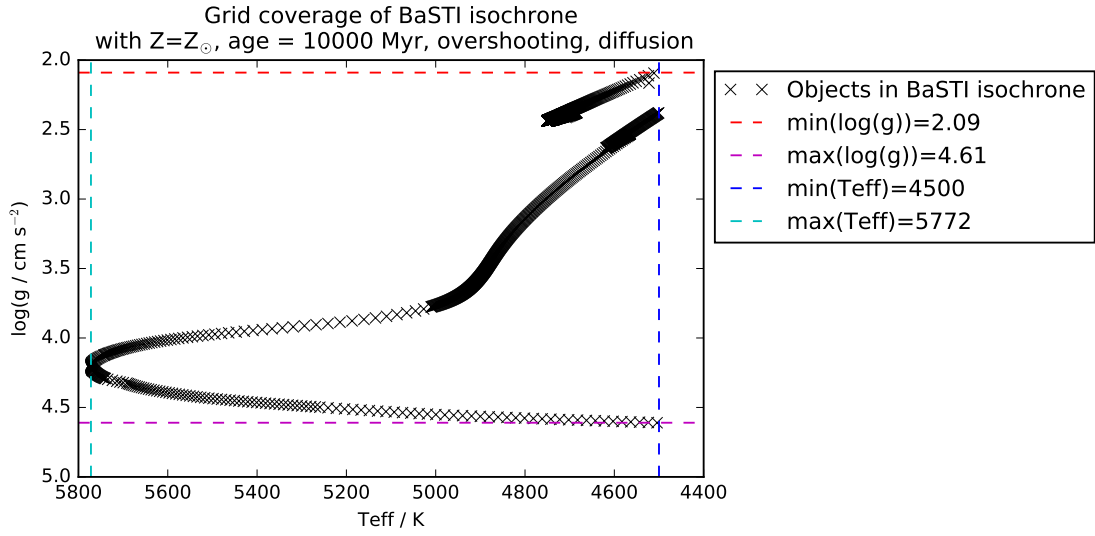


Figure 4.8: $T_{\text{eff}}\text{-log}(g)$ grid coverage by a 10 Gyr, Z_{\odot} BaSTI isochrone including mass-loss, core overshooting and diffusion effects

Chapter 5

Future work

This work, although confirming feasibility of thermohaline mixing in BaSTI, has yet to implement the effects of the resultant chemical mixing on the models of the star at times following the initial mixing. The next step should be to integrate the conditions for thermohaline mixing into the relevant BaSTI routines allow local chemical compositions to change in response to thermohaline mixing, which in turn allows the mixing effect to propagate into the radiative zone, the first step that must be taken if the mixing is to have any impact on observable (surface) chemical abundances.

The accuracy of the results of a full implementation of thermohaline mixing into BaSTI will still be unclear, given the known impact of rotation (Collins (1963) Maeder & Zahn (1998), Matrozis & Stancliffe (2017), Ekström et al. (2012)) and radiative levitation (Matrozis & Stancliffe, 2016) on stellar interior structure, and hence on observed emission, both in single stars and populations. For example, rotation is a possible explanation for the phenomenon of extended main sequence turnoffs (Niederhofer et al. (2015), Bastian et al. (2016)), split main sequences and multiple populations.

When combining multiple diffusive effects, it is common to treat the effects as independent, such that the combined effect, described by a coefficient $D_{tot} = \sum_i D_i$, is the sum total of the individual effects. Maeder et al. (2013), studying the general stellar case, found that the general stability criterion as a function of D_{tot} involves coupling of multiple effects. This coupling will need to be considered when adding new effects to BaSTI, particularly rotation.

For differential extinction, the immediate goal is to derive A_1 and A_2 functions that are sufficiently accurate. The final step will be to apply them to the isochrone data by using the values of T_{eff} and $\log(g)$ for each object in a given isochrone, together with the Z value of the isochrone and the unique coefficients for each filter. The resulting extinction will then be added to the filter magnitude data for the objects and colour-magnitude diagrams (CMDs) will be plotted, simulating an observed stellar population, to study any differences in the distribution of the objects. The final step will be to compare the results with observed populations in the same CMD.

The ultimate goal of this PhD, and of the field of stellar physics in general, is to predict, quantitatively and accurately, the evolution of a star and, particularly,

its fundamental observable properties over the course of its lifetime. This requires all known potential sources of mixing and instability to be factored into a single framework. This project will attempt to work towards this goal in BaSTI.

5.1 Timeline

- September 2018 - January 2019: Finish extinction fitting, study the effects on isochrones and Write up and submit these results.
- January - April 2019: Write the full routine in BaSTI to implement thermohaline mixing.
- April - July 2019: Study the effects of thermohaline mixing on low-mass BaSTI stellar models, in particular the surface chemical mass-fractions, compare with calculations from other models and publish results.
- July 2019 - March 2020: Implement routines in BaSTI governing the effects of stellar rotation, compare with calculations from other models. Write up and submit results of this analysis.
- March 2020 - July 2020: Compare the results of the rotating BaSTI models with results inferred from objects observed to host multiple population, extended main-sequence turnoffs or split main sequence phenomena.
- July - December 2020: Implement routines in BaSTI governing the effects of radiative levitation, compare with calculations from other models.
- December 2020 - March 2021: Compare the results of all new effects to observations of globular cluster turnoffs and horizontal branch stars.
- March - May 2021: Write up and submit 2 papers about the results of the combined effects on BaSTI.
- April - October 2021: Write up and submit PhD thesis.

Bibliography

- Angelou G. C., Church R. P., Stancliffe R. J., Lattanzio J. C., Smith G. H., 2011, *ApJ*, 728, 79
- Angelou G. C., Stancliffe R. J., Church R. P., Lattanzio J. C., Smith G. H., 2012, *ApJ*, 749, 128
- Bastian N., et al., 2016, *MNRAS*, 460, L20
- Cantiello M., Langer N., 2010, *A&A*, 521, A9
- Cardelli J. A., Clayton G. C., Mathis J. S., 1988, in *ESA Special Publication*.
- Cardelli J. A., Clayton G. C., Mathis J. S., 1989, *ApJ*, 345, 245
- Casagrande L., VandenBerg D. A., 2018a, *MNRAS*, 475, 5023
- Casagrande L., VandenBerg D. A., 2018b, *MNRAS*, 479, L102
- Castelli F., Kurucz R. L., 2004, *ArXiv Astrophysics e-prints*
- Castelli F., Gratton R. G., Kurucz R. L., 1997, *A&A*, 318, 841
- Charbonnel C., Zahn J.-P., 2007, *A&A*, 467, L15
- Collins II G. W., 1963, *ApJ*, 138, 1134
- Denissenkov P. A., 2010, *ApJ*, 723, 563
- Eggleton P. P., Dearborn D. S. P., Lattanzio J. C., 2006, *Science*, 314, 1580
- Ekström S., et al., 2012, *A&A*, 537, A146
- Fitzpatrick E. L., Massa D., 1988, *ApJ*, 328, 734
- Girardi L., et al., 2008, *PASP*, 120, 583
- Hidalgo S. L., et al., 2018, *ApJ*, 856, 125
- Kippenhahn R., Ruschenplatt G., Thomas H.-C., 1980, *A&A*, 91, 175

- Kurucz R., 1993, ATLAS9 Stellar Atmosphere Programs and 2 km/s grid. Kurucz CD-ROM No. 13. Cambridge, Mass.: Smithsonian Astrophysical Observatory, 1993., 13
- Lattanzio J. C., Siess L., Church R. P., Angelou G., Stancliffe R. J., Doherty C. L., Stephen T., Campbell S. W., 2015, MNRAS, 446, 2673
- Maeder A., Zahn J.-P., 1998, A&A, 334, 1000
- Maeder A., Meynet G., Lagarde N., Charbonnel C., 2013, A&A, 553, A1
- Matrozis E., Stancliffe R. J., 2016, A&A, 592, A29
- Matrozis E., Stancliffe R. J., 2017, A&A, 606, A55
- Moore K., Garaud P., 2016, ApJ, 817, 54
- Niederhofer F., Georgy C., Bastian N., Ekström S., 2015, MNRAS, 453, 2070
- Ortolani S., Cassisi S., Salaris M., 2017, Galaxies, 5, 28
- Pasian F., Taffoni G., Vuerli C., Manzato P., Gasparo S. F. C., Pietrinferni A., Salaris M., 2008, in Argyle R. W., Bunclark P. S., Lewis J. R., eds, Astronomical Society of the Pacific Conference Series Vol. 394, Astronomical Data Analysis Software and Systems XVII. p. 285
- Pietrinferni A., Cassisi S., Salaris M., Castelli F., 2004, ApJ, 612, 168
- Pietrinferni A., Cassisi S., Salaris M., Hidalgo S., 2013, A&A, 558, A46
- Salaris M., Cassisi S., 2005, Evolution of Stars and Stellar Populations
- Salaris M., Cassisi S., 2017, Royal Society Open Science, 4, 170192
- Savage B. D., Mathis J. S., 1979, ARAA, 17, 73
- Ulrich R. K., 1972, ApJ, 172, 165